

The syncytial *Drosophila* embryo as a mechanically excitable medium

Timon Idema^{1,*}, Julien O. Dubuis², M. Lisa Manning³, Philip C. Nelson¹, Andrea J. Liu^{1,†}

1 Department of Physics and Astronomy, University of Pennsylvania, Philadelphia, PA, USA

2 Department of Physics, Princeton University, Princeton, NJ, USA

3 Department of Physics, Syracuse University, Syracuse, NY, USA

*** Present address: Department of Bionanoscience, Delft University of Technology, Delft, The Netherlands; E-mail: t.idema@tudelft.nl**

† E-mail: ajliu@sas.upenn.edu

Abstract

Mitosis in the early syncytial *Drosophila* embryo is highly correlated in space and time, as manifested in mitotic wavefronts that propagate across the embryo. In this paper we investigate the idea that the embryo can be considered a mechanically-excitable medium, and that mitotic wavefronts can be understood as nonlinear wavefronts that propagate through this medium. We study the wavefronts via both image analysis of confocal microscopy videos and theoretical models. We find that the mitotic wavefront can be resolved into two distinct wavefronts in each cycle, corresponding to metaphase and anaphase, respectively. The two wavefronts have the same speed and are separated by a time interval that is independent of cycle, supporting the idea that they are two different markers for the same process. To understand the wavefronts theoretically we analyze wavefront propagation in excitable media. We study two classes of models, one with biochemical signaling and one with mechanical signaling. We find that the dependence of wavefront speed on cycle number is most naturally explained by mechanical signaling, and that the entire process suggests a scenario in which biochemical and mechanical signaling are coupled.

1 Introduction

The early embryos of many species, including *Drosophila* [1–3], *Xenopus* [4–6], *Oryzias* [7], *Fundulus* [8], and zebrafish [9, 10], exhibit metachronous mitosis, in which mitosis progresses as a wavefront through the embryo. Such wavefronts are reminiscent of biochemical wavefronts that are used to transmit signals across many cells in other biological systems, such as wavefronts of the molecule cAMP that propagate in a colony of *Dictyostelium* when it begins to aggregate to form a fruiting body [11–13]. Propagating wavefronts, however, need not be purely biochemical in origin. The process of mitosis is a highly mechanical one that involves significant changes in the volume occupied by chromatin [14] as well as separation of chromosomes [15]. This raises the question of whether mitotic wavefronts are purely biochemical phenomena or whether they might have a mechanical component as well.

The nuclei of the *Drosophila* embryo are syncytial (i.e., they share the same cytoplasm and are not separated into individual cells by plasma membranes) during their first thirteen division cycles. The nuclei migrate to the egg's surface during the ninth cycle. There they divide five more times, until the fourteenth cycle, when cell membranes form and gastrulation begins [1]. Mitotic wavefronts are observed in cycles 9 through 13 [1]. In this period, chemical diffusion is unhindered by membrane barriers. It is known that calcium, a signal carrier that influences many local phenomena including mitosis [16–18], exhibits localized waves or spikes of concentration in the syncytial embryo [19–23]. The observation by Parry et al. [20] that there is a calcium wavefront in each cycle that travels across the embryo at the same speed as the mitotic wavefront, and occurs near the onset of anaphase, suggests that calcium signaling may be responsible for the mitotic wavefront.

However, mitosis is also a mechanical phenomenon. In the syncytial embryo, nuclei are embedded in

an elastic cytoskeleton, which contains both actin and microtubules [24–26]. Actin caps assemble around each of the nuclei at the end of interphase, and provide anchor points for the mitotic spindles that pull the two daughter nuclei apart [24–27]. Recent work shows that mechanical interactions are important for re-organization of the nuclei after mitosis [28], and optical tweezer experiments show that nuclei are mechanically coupled [29]. However, little is known about how mechanical interactions affect collective phenomena such as mitotic wavefronts at the level of the entire embryo.

In this paper we report the results of both our image analysis of wavefronts in early *Drosophila* embryos, and our theoretical studies of models of wavefront propagation. Using novel tracking techniques, we analyzed confocal microscopy videos taken of *Drosophila* embryos in which the nuclear DNA/chromosomes are visualized by labeling their histones with GFP. Our analysis yields the position, shape and dynamics of the DNA/chromosomes with high temporal and spatial resolution during cycles 9–14. We observe two distinct wavefronts in each cycle, one corresponding to the onset of metaphase (at which point the chromosomes condense in the nuclear midplane, known as the metaphasic plate - see figure 4 for an illustration of the different stages) and one corresponding to the onset of anaphase. To our knowledge, the metaphasic wavefront has not been observed before. We find that for a given cycle in a given embryo, the metaphasic and anaphasic wavefronts have the same speed, which remains constant as they propagate across the embryo. Moreover, for a given embryo, the time between the two wavefronts is always the same, consistent with the view that the onsets of metaphase and anaphase can be viewed as different markers of the overall process of mitosis. Both wavefronts slow down with cycle, and produce large-scale collective motion of the nuclei.

We treat the embryo theoretically as an excitable medium, consisting of nuclei that can be triggered into initiating metaphase or anaphase, thereby locally exciting the medium and thus signaling their neighbors. We not only consider the well-known case of nonlinear wavefront propagation in a chemically excitable medium [30,31], but introduce a model for the early embryo as a *mechanically* excitable medium [32], through which mitotic wavefronts can propagate via stress diffusion. Comparing the data with the results of these two models, we find that our observations are difficult to reconcile with a purely biochemical scenario. In such a scenario, the wavefront speed has a tendency to *increase* with nuclear density, and thus with cycle, contrary to our observations. The observations can, however, be explained quite naturally by a novel scenario in which nuclei not only respond to their mechanical environment, but also actively use it to signal each other. Our results suggest that mitotic wavefronts in syncytial *Drosophila* embryos may constitute one example of a previously unexplored form of mechanical signaling via nonlinear wavefronts that could also arise in very different biological contexts [32,33].

2 Results

2.1 Image analysis results

Nuclear cycle and shape

An example image of detected nuclei in a *Drosophila* embryo is shown in figure 1a. In each cycle, as the nuclei progress from interphase through metaphase to anaphase, the detected shape of the DNA/chromosomes changes in a well-defined manner (figure 1b). Newly separated nuclei are small and spherical, and thus show up in our shape tracking as small circles. During interphase, the nuclear DNA grows in size over time as it is duplicated. At the onset of metaphase, the chromosomes condense in the midplane of the nucleus, and appear to elongate into an ellipse. The final step of mitosis, the onset of anaphase, corresponds to two detectable changes in the shape: a sudden shift of the orientation axis over a $\pi/2$ angle, and a change of aspect ratio. An example plot showing the ratio of the length of the two axes as a function of time during a cell cycle is given in figure 1c.

Metaphasic and anaphasic wavefronts

The onsets of metaphase and anaphase, as determined by the axes ratio (figure 1d) are indicated by dotted blue lines and dashed orange lines, respectively. Evidently the onset of metaphase forms two wavefronts, one propagating from each pole (not necessarily starting at the same time); the displacements of the chromosomes follow these wavefronts. Similarly, the onset of anaphase forms two wavefronts, also causing chromosomal displacements. Mitotic waves were first observed by Foe and Alberts [1]; with better time resolution, it is evident that instead of a single mitotic wavefront in each cycle, there are two distinct wavefronts corresponding to the onsets of metaphase and anaphase. There may be additional wavefronts that cannot be resolved from the axes ratio or chromosomal displacements.

Effect of shape changes on nuclear positions

The processes of metaphase and anaphase affect not only the shapes of the chromosomes, but also their positions. After each of the shape changes, the nuclei move *collectively* through the embryo, almost exclusively along the long axis (which we designate as the x -axis), resulting in a global ‘breathing mode’ of the entire embryo (see SI movie 1 [34]). Remarkably, after an initial transition in which the nuclei re-organize after anaphase, the nuclei hardly move with respect to their nearest neighbors during this collective movement. Figure 1e shows the average displacement Δx along the x -axis of a small set of nuclei. Figure 1f shows the same motion for all nuclei, illustrating that the metaphasic and anaphasic wavefronts are reflected in corresponding wavefronts in the mechanical response.

Wavefront speeds

We quantify the wavefront speeds in figure 2 for two sets of movies, where the environmental conditions (in particular the temperature) are approximately the same for all movies in a given set, but different from one set to the other (the data of the two sets were taken several months apart). Figure 2a shows an example of a position vs. time plot of all condensation (blue diamonds) and anaphase (red pluses) events in a single cycle. The slope, corresponding to the wavefront speed, is clearly constant across the embryo. Figure 2b shows the ratio of the speeds of the anaphasic and metaphasic wavefronts, showing that for a given embryo and cycle, the two wavefronts move at the same speed. From embryo to embryo there are large variations in wavefront speed (figure 2c), but they all show the same exponentially decaying trend. This trend is illustrated in figure 2e, where we plot the same data, normalized by the speed of the first wavefront, on a log-linear scale. Figure 2d shows that the time interval that separates the metaphasic from the anaphasic wavefront is the same for all cycles for a given embryo, but is different for the two different sets of data. By looking at the point at which the nuclear envelope breaks down and reforms, Foe and Alberts [1] also found that the duration of the mitotic phase is constant through cycles 10, 11 and 12 (3 minutes in their observations, comparable to our result), but was longer for cycle 13 (5 minutes). The re-formation of the nuclear envelope membrane may therefore take significantly longer in the last syncytial cycle, even though the actual wavefronts keep following the pattern of the earlier cycles.

Cycle statistics

The nuclei on the surface are separated by a well-defined distance a_n , which decreases with cycle number n . Because the number of nuclei doubles from one cycle to the next, it is not surprising that a_n decays exponentially, scaling like $a_n \sim 2^{-\beta(n-n_0)}$, with n the cycle number and n_0 the number of the first observed cycle. We consistently found a value of $\beta = 0.46$ in our experiments (figure 2f and table 1). The value of β is slightly less than $1/2$, presumably because the curved embryo is being projected onto a plane. We have also measured the duration of each cycle, t_n , and found that it increases with cycle number n , with a weak exponential growth: $t_n = t_0 e^{0.29 \cdot n}$, where ($t_0 = 33$ s for set 1 and $t_0 = 25$ s for set 2, see table 1 and figure 7).

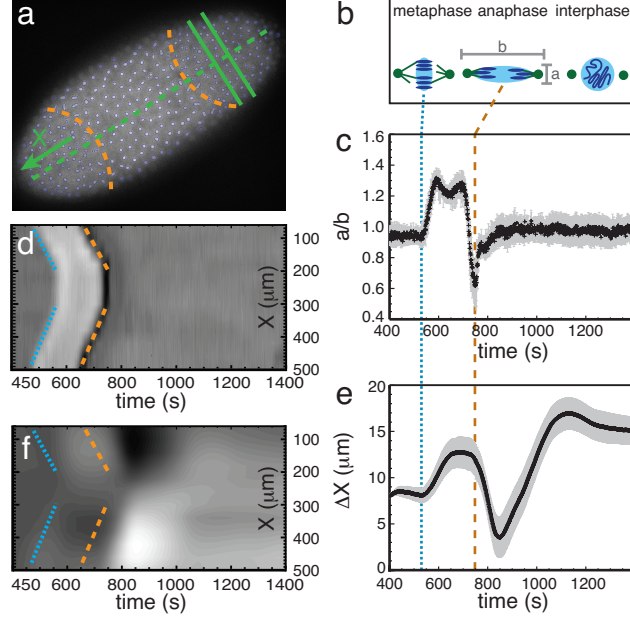


Figure 1. Observation of wavefronts and mechanical response. a) Image of a *Drosophila* embryo during mitosis at the end of cycle 11, with the detected chromosomal contours overlaid. Anaphasic wavefronts (orange dashed curved lines), the long axis (green dashed straight line) and a typical slice perpendicular to the long axis (green parallel straight lines) are indicated. b) Sketch of the three main states in image analysis: interphase (circular contours), metaphase (compressed elliptical contours), and anaphase (highly extended elliptical contours, perpendicular to metaphase contour). See also figure 4. c) Ratio of the two elliptical axes of the detected shape of the nuclear DNA/chromosomes vs. time in cycle 11, averaged over an x -slice (as shown in a); error bars indicate variation within the slice. The transitions between interphase and metaphase, as well as the onset of anaphase, are sharp and indicated respectively by dotted (blue) and dashed (orange) vertical lines. The slice shown was taken at $x = 200\mu\text{m}$. d) Kymograph showing the elliptical axes ratio, a/b (where white indicates values larger than 1 and black indicates values smaller than 1), as a function of position x and time. The dotted and dashed lines indicate the two wavefronts. e) Average x -displacement Δx of the nuclei within one slice vs. time. After a nucleus has divided, we use the average position of its two daughters. The slice shown is identical to the one in figure c. f) Kymograph showing the collective motion of nuclei in slices taken at different positions along the long axis of the embryo. White indicates motion in the positive x direction, black in the negative x direction. Dotted and dashed lines again indicate the two wavefronts.

2.2 Theoretical Analysis

Our observation that the metaphasic and anaphasic wavefronts propagate at constant speed across the embryo suggests that the embryo can be considered as an excitable medium that supports nonlinear front propagation. Alternatively, the nuclei could all have biological clocks that determine when mitosis starts, which operate independently; in that case the wavefront would be only a result of a lucky timing of those clocks. We briefly discuss various timing models below, and show that these are inconsistent with our observed data, so we conclude that the nuclei do communicate. We have considered two distinct classes of models for front propagation in excitable media. In the first model the nuclei communicate by releasing a small chemical, which then diffuses to neighboring nuclei, triggering them to initiate metaphase or

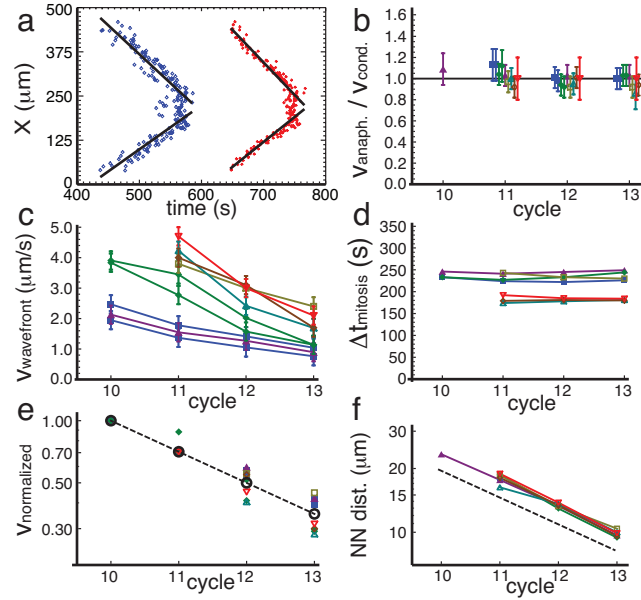


Figure 2. Wavefront propagation and speeds. a) x -coordinate of nuclei at the onset of metaphase (blue diamonds) and anaphase (red pluses) vs. time for the wavefront shown in figure 1. Both events show two clear wavefronts moving in from near the embryo poles (solid lines). b) Ratio of the speeds of the metaphasic and anaphasic wavefronts for different embryos and cycles. Each embryo is indicated by a different symbol and color, with the closed and open symbols representing two different measurement sets. Ratios for a given cycle and different embryos are slightly separated horizontally. c) Wavefront speed vs. cycle. Two of the embryos contribute two waves per cycle (coming in from opposite poles, as in figure 1a; blue squares and green diamonds). Although the actual propagation speeds vary significantly from one embryo to the next, they all follow the same trend, decreasing with successive cycles. d) Time interval between the metaphasic and anaphasic wavefronts vs. cycle. e) Log-linear plot of wavefront speeds vs. cycle, normalized by the speed of its first occurring wave front (if the first wave front is in cycle 10) or 0.71 times its first occurring wavefront (if the first wave front is in cycle 11). The black open circles connected by a dashed line corresponds to a scaling of 0.71 per cycle, showing that all embryos follow the same exponentially decaying trend. f) Average distance between nearest neighbors on a logarithmic plot. The dashed line has a slope of 0.46. In figures b-f, the same symbol/color corresponds to the same embryo.

anaphase. In the second model we explore the novel idea that mitotic wavefronts in the early embryo can be described by wavefront propagation in a medium that is *mechanically* rather than *chemically* excitable. In this model, the deformation of nuclei during metaphase or anaphase gives rise to mechanical stresses that trigger other nuclei to proceed to that phase as well.

Timing models

Consider the following timing mechanism for generating a wavefront in a row of people. Assume each person has a (synchronized) watch, and each is told to raise his/her arms at a constant time interval apart. If the clock of each successive person in the row runs a little slower than that of the previous person, and they all raise their arms when their local clock reaches a certain agreed upon time, a wavefront will be generated.

For the timing method to be the cause for the wavefronts observed in our system, each nucleus would require a clock. That clock could simply be the amount of time it takes to duplicate the DNA, i.e., the duration of the interphase, which changes from one cycle to the next. However, there is no correlation between a nucleus' position and the duration of interphase, which means that we would not expect a mitotic wavefront to emerge in this case. Alternatively, it is well-established that there are several proteins which exhibit patterning along the anterior-posterior or dorsal-ventral axes of the embryo. A much studied example is Bicoid, which exhibits an exponential profile along the anterior-posterior axis [35,36], the same axis along which the wavefront travels. Now if the duration of interphase were affected by the local Bicoid concentration, that could provide a mechanism for the clocks of the nuclei to get out of sync, and produce a wavefront in the various markers for mitosis (such as our observed metaphase and anaphase wavefronts).

There are three reasons why the model outlined above cannot explain our data. The first is specific to Bicoid. As observed by Gregor et al. [36], the total amount of Bicoid steadily increases over time, as more of the protein is translated in each cycle. In particular, the amount of protein keeps steady pace with the number of nuclei, such that at the start of each cycle, the actual amount of protein in each nucleus at a given position in the embryo is always the same. Therefore if Bicoid were responsible for causing the mitotic wavefronts, the wavefronts would have the same speed in each cycle, which they do not. The second reason is more general: as shown in appendix D, in order to obtain a linear wavefront propagation from an exponential concentration profile, the actual absolute amount of material does not matter, only the decay length - which means that once again the predicted wavefront speed would be independent of cycle. Finally note that to get wavefronts traveling in both directions along the anterior-posterior axis of the embryo, we would need at least two concentration gradients of different proteins, for which it would be highly surprising if they produced wavefronts with the same speed. The timing method therefore cannot describe our data.

Biochemical-signaling model

At the end of a cycle, when all nuclei have completed the duplication of their DNA, we assume that they are in an excitable state, meaning that they can be triggered to initiate mitosis once they receive an appropriate signal. An obvious candidate for signaling between nuclei is the diffusion of a small ion, molecule or protein (*e.g.* calcium, cyclic AMP, Bicoid), which we will denote as A . By definition, nuclei can divide only once per cycle; therefore, in our model, we introduce a refractory period for each nucleus following anaphase, equal to the duration of the interphase.

To introduce chemical excitability, we assume that if the local concentration of A exceeds a threshold α , the nucleus starts its program of mitosis, part of which involves releasing more A . A then diffuses away, raising the concentration of A at neighboring nuclei, and so on. In our model we also allow for a time delay t_{delay} between trigger and release, meaning that a nucleus does not release more A until a time t_{delay} after its local concentration exceeds α . We model releases of A by the nuclei (or sources) as localized pulses (Dirac delta functions), and the system is initiated with a single nucleus releasing A . The wavefront at any point in time corresponds to the position of all nuclei that release A at that moment. Details on how to solve the diffusion equation and carry out the other needed calculations are given in appendices E and G. An example wavefront is shown in figure 3a.

The speed v of the resulting wavefront is determined by three parameters: the diffusion constant D , the nuclear spacing a and the concentration threshold α . Because our system is effectively two-dimensional, α has dimensions of $1/\text{length}^2$. We obtained the value of a from direct measurements. Gregor et al. [37] found from diffusion experiments in *Drosophila* that the diffusion constant of a molecule with hydrodynamic radius R is well described by a modified Stokes-Einstein relation [38]: $D = k_B T / (6\pi\eta R) + b$, where k_B is Boltzmann's constant, T the temperature, $\eta = 4.1 \pm 0.4\text{cP}$ the effective viscosity of the syncytial *Drosophila* embryo, and $b = 6.2 \pm 1.0\mu\text{m}^2/\text{s}$ is an experimentally determined constant. Using this expression, we estimate that a calcium ion with a radius of approximately 0.5nm has a diffusion constant of about $10^2\mu\text{m}^2/\text{s}$. We have no direct way of estimating the threshold α , so we solved the

model numerically for a range of values of α .

Combining the parameters of our model, we define a nondimensional threshold, $\bar{\alpha} = 4\pi a^2 \alpha$ and speed $\bar{v} = \frac{v}{D/a}$. As shown in appendix E, we then have $\bar{v} = 1/f(\bar{\alpha})$, where $f(\bar{\alpha})$ increases monotonically with $\bar{\alpha}$ (figure 11). Consequently, if both D and α are fixed, the wavefront speed v increases as the nuclear spacing a decreases, and thus the speed increases with cell cycle, in direct contradiction to our experimental observations. Moreover, numerically solving for the wavefront in this model shows that the resulting wave speeds are much larger than the ones we observed in the experiments, by up to two orders of magnitude in the later cycles (see figure 10). For a different chemical with a smaller diffusion constant we find that the magnitude of the predicted speed is closer to the experimental value, but the trend (increasing speed with cycle) persists. Thus, the simplest form of the biochemical signaling model cannot describe the data of figure 2c.

We next consider the possibility of a delay t_{delay} between the time when the local concentration of A reaches the threshold value α , and the instant when more A is released. For details on the implementation see appendix G.2. In the limit where $a^2/D \gg t_{\text{delay}}$, the wavefront speed is determined by diffusion as before, $v = D/(af(\bar{\alpha}))$. In the opposite limit, $a^2/D \ll t_{\text{delay}}$, we find $v = a/t_{\text{delay}}$, so v would decrease with cycle number for constant t_{delay} . However, we find that to get the correct speeds in the earlier cycles requires a delay time of 5-10s, which is comparable to a^2/D for calcium; for this range of delay times, the speed still increases with cycle number (blue diamonds in figure 3c). Only for much larger delay times of 100s or more do we arrive at the regime where $v = a/t_{\text{delay}}$, but then the speeds we obtain are much lower than those we measured experimentally. Again, for a chemical with a smaller diffusion constant, the trend remains the same; in that case a^2/D is larger, and we move further into the diffusion-dominated regime. Thus, a biochemical-signaling model with a time delay that is independent of cell cycle cannot describe our observations either.

We also investigated the wavefront speed in the case where the delay time is allowed to vary from one cycle to the next. Since the cycle duration shows a weak exponential increase with cycle number (figure 7), we might speculate that the delay time also increases exponentially. However, as shown in figure 10 (red points), this dependence cannot explain the experimental data either. As stated above, a diffusion constant $D = 10^2 \mu\text{m}^2/\text{s}$ requires a delay time of 5-10s to fit the wavefront speed in the first observed cycle; however, the last cycle then requires a delay time of approximately 10^3s , which is comparable in length to the entire cycle and much longer than the duration of mitosis. We therefore consider smaller diffusion constants, although those would imply larger signaling molecules which have not been identified. In the case that $D = 10 \mu\text{m}^2/\text{s}$ (almost the lower limit for which we can still fit the speed of cycle 10), we can fit the data only if we allow the delay time to vary freely from one cycle to the next (see table 2). However, we do not find a systematic dependence of the delay time on the cycle; moreover, even though the required delay time is now shorter than the duration of mitosis, in the latter cycles it is still significantly larger than the time it takes the wavefront to travel from one nucleus to the next. Consequently, whereas in the early cycles we would have simple neighbor-neighbor interactions, in the latter cycles there would be interactions between nuclei that are 4 or 5 rows apart. More details on this are given in appendix E. There, we also analyze the possibility that the concentration threshold changes with cycle, and find that in order to fit the data, it has to change by four orders of magnitude. Even changing both t_{delay} and α does not resolve these problems (table 2).

On the basis of these results, we conclude that a wavefront that propagates via diffusion of calcium should not slow down with cycle number. It is possible that a wavefront of a larger biomolecule with a lower diffusion coefficient could do so, although this is also unlikely and no such species has been identified. We also note that any model in which the biochemical signal is mediated by a method that is faster than diffusion (such as active transport) suffers from the same problem: the predicted wavespeed would go up with increasing cycle, because the spacing between the nuclei goes down.

Mechanical-signaling model

The early embryo cannot support ordinary elastic waves because it is heavily damped by the viscosity of the cytosol. Consequently, displacements do not propagate ballistically as in a wave, but diffusively. However, just as diffusion of A can lead to wavefront propagation in the biochemical signaling model, diffusion of displacement could lead to wavefront propagation in a mechanical signaling model. We therefore introduce a model in which the nuclei communicate via stresses or strains that they exert on the cytoskeleton when they undergo condensation or anaphase. In this model, a nucleus starts its mitotic program when the largest eigenvalue of the local stress tensor exceeds a threshold value α . We describe the cytoskeleton as a homogeneous linear elastic medium, characterized by two elastic parameters, for example its bulk and shear moduli (K and μ , respectively) or the Young's modulus E and dimensionless Poisson ratio ν . The viscous fluid in which the elastic cytoskeleton is immersed exerts a drag force on it, characterized by a damping constant Γ . Assuming that the nuclei exist in a thin layer near the surface of the embryo, we denote the deformations in the plane of the layer by $u_i = x'_i - x_i$ ($i = 1, 2$), when the deformation maps point (x_1, x_2) onto point (x'_1, x'_2) . The displacement \vec{u} of a nucleus can be described by [39]:

$$\Gamma \partial_t u_i = \frac{E}{2(1+\nu)} \partial_j \partial_j u_i + \frac{E}{2(1-\nu)} \partial_i \partial_j u_j. \quad (1)$$

The term on the left represents the damping with damping factor Γ , and the two terms on the right are the elastic force. Equation (1) is reminiscent of the diffusion equation: a time derivative on the left equals second-order space derivatives plus a source term on the right. This model can therefore be thought of as describing the diffusion of the vector displacement field u_i . The right hand side of equation (1) gives rise to two quantities with the dimensions of diffusion constants [32]:

$$D_1 = \frac{E}{(1-\nu^2)\Gamma} = \frac{1-\nu}{2} \frac{\mu}{\Gamma} \quad \text{and} \quad D_2 = \frac{E}{2(1+\nu)\Gamma} = \frac{\mu}{\Gamma}. \quad (2)$$

In order to introduce *mechanical excitability* into the model, we assume that if the largest eigenvalue of the stress tensor at a nucleus at position \vec{x}_0 exceeds a threshold value, α , at time t_0 , it triggers a force dipole, adding another term $\partial_j Q_{ij} \delta(\vec{x} - \vec{x}_0) \Theta(t - t_0)$ to the right hand side of equation (1):

$$\Gamma \partial_t u_i = \frac{E}{2(1+\nu)} \partial_j \partial_j u_i + \frac{E}{2(1-\nu)} \partial_i \partial_j u_j + \partial_j Q_{ij} \delta(\vec{x} - \vec{x}_0) \Theta(t - t_0), \quad (3)$$

where Q_{ij} is a symmetric tensor of rank 2. Here $\delta(\vec{x})$ is the two-dimensional Dirac delta function and $\Theta(t)$ is the Heaviside step function. Equation (3) essentially describes the diffusion of the vector displacement field u_i due to a tensor source term. It is similar, but not identical, to a scalar reaction-diffusion equation, which describes the evolution of a scalar concentration field c due to a scalar source term. It is therefore not surprising that the model described by equation (1) also produces wavefronts, as can be seen in figure 3b.

In order to compare the model results with the data, we need to estimate the values of the elastic constants and the damping parameter. The speed v now depends on the quantity $D = \mu/\Gamma$ that determines the dimensional part of both diffusion constants (equation (2)), as well as the nuclear spacing a and the threshold value α . Following Palmer et al. [40], we estimate the shear modulus of our elastic network to be of the order of 1–10 Pa. The damping parameter Γ is the drag per unit volume, which for a mesh of semiflexible polymers should be roughly equal to the number of filaments times the drag on each of them: $\Gamma \sim c\eta l_{\text{mesh}} \sim \eta/l_{\text{mesh}}^2$, where c is the filament concentration, l_{mesh} the mesh size and η the viscosity of the surrounding fluid. For $\eta \sim 4 \cdot 10^{-3} \text{ Pa} \cdot \text{s}$ and $l_{\text{mesh}} \sim 100 \text{ nm}$, we find that $D \sim 5 - 20 \mu\text{m}^2/\text{s}$.

The elastic moduli and the damping parameter should depend both on frequency (which is low in our case) and local filament concentration [40–44], which can differ from one cycle to the next. Because the number of nuclei doubles in each cycle, the number of actin caps making up the network doubles as

well (see figures 4 and 5). Thus, the local concentration of actin and of microtubules should effectively double with cycle number n . We therefore write $c \sim 2^{(n-n_0)}$, where as before n_0 is the number of the first observed cycle. Both the storage and loss moduli of polymer networks increase with concentration approximately as power laws, but the actual powers are debated [40, 42–44]. Moreover, in each successive cycle the nuclei get pushed further out into the plasma membrane encompassing the entire embryo [1], increasing the friction coefficient. Because the dynamics of our system depends only on the value of the two effective diffusion constants given in equation (2), we will not be able to distinguish the dependence of the storage and loss moduli independently. Instead we assume a dependence $D = \mu/\Gamma \sim c^{-\gamma} \sim 2^{-\gamma(n-n_0)}$.

Because of the mathematical similarity between the mechanical-signaling model (equation (1)) and the diffusion model for concentration fields, we use the same type of dimensional analysis as for the diffusion-signaling model and write $v = (D/a)g(\bar{\alpha}, \nu) = (\mu/a\Gamma)g(\bar{\alpha}, \nu)$, where now $\bar{\alpha} = a^2\alpha/Q$, with Q the magnitude of the force dipole and a the spacing between the nuclei. We determine $g(\bar{\alpha}, \nu)$ numerically, and find that it can be well described by the functional form $g(\bar{\alpha}, \nu) = -4(1 - \bar{\alpha}) \log(\bar{\alpha})/(1 - \nu)$ [32]; for details, see the appendix G.3. We now consider two possibilities. First, the value of the dimensionless threshold $\bar{\alpha}$ can be constant throughout stages 9–14, which means that the individual nuclei are effectively the same in all cycles, adapting for the change in polymer density and available area. It is well known in the literature that such adaptive patterns are present in, for instance, expression patterns of morphogen proteins like Bicoid [36], where the total amount of Bicoid increases in such a manner that the amount per nucleus remains the same. It is conceivable that something similar happens with the stress threshold α , causing the dimensionless version $\bar{\alpha}$ to be constant. If this is the case, the wavefront speed only scales with the prefactor $\mu/a\Gamma$, which itself depends on the cycle as $2^{(\beta-\gamma)(n-n_0)}$, using the experimental result that $a = a_0 \cdot 2^{-\beta(n-n_0)}$. For this case we find from fitting the experimental data that $\gamma = 1.0$ (green fits in figure 3d). The second possibility is that the actual stress threshold value α is constant, and thus $\bar{\alpha}$ scales like $2^{-2\beta(n-n_0)}$. We then use our functional form for $g(\bar{\alpha}, \nu)$ to fit the experimental data, and find that $\gamma = 1.4$ and $\alpha = 0.1 \cdot Q$, where Q is the strength of the force dipoles (blue lines in figure 3d). Note that in both cases we need to set the absolute scale, i.e., the wavefront speed in the first fitted cycle; this value v_0 absorbs the values of μ , Γ and a in the first fitted cycle as well as the factor $1 - \nu$ in the denominator of our functional form. However, once v_0 is determined for each dataset, the same fit parameters (γ for fixed $\bar{\alpha}$ and γ and α for fixed α) describe both sets of data, indicating that the trend is the same. In both cases ($\bar{\alpha}$ constant and α constant) we find a good fit; we can therefore at present not distinguish between the two possibilities. Further experiments, such as ones in which the embryo is poked mechanically with a well-controlled force (see Discussion), are needed to resolve this issue.

The value for γ obtained above is reasonable for crosslinked semiflexible networks. For a semidilute solution of rigid rods, the viscosity is expected to rise as c_A^3 , where c_A is the filament concentration [45]. The modulus of a semiflexible network should scale as $l_{\text{mesh}}^{-2} l_{\text{ent}}^{-3}$, where l_{mesh} is the mesh size and l_{ent} is the filament entanglement length [46]. For a crosslink concentration c_x , one would expect $l_{\text{mesh}} \sim l_{\text{ent}} \sim c_x^{-1/3}$, leading to $\mu \sim c_x^{5/3}$. For the damping coefficient Γ we obtain $\Gamma \sim c_A \eta l_{\text{mesh}} \sim c_A^4 c_x^{-1/3}$. In each cycle, we would expect $c_x \propto c_A$, that is, the local concentrations of all biomolecules, actin and crosslinker proteins included, should increase proportionately. This would lead to $D = \mu/\Gamma \sim c_A^{-2}$, so that $\gamma = 2$, in reasonable agreement with $\gamma \sim 1.4$. We note that it would be valuable to measure experimentally the actin concentration near the embryo surface as a function of cell cycle to pin down these estimates more precisely.

3 Discussion

During the early cycles of *Drosophila* development, the cycles of the nuclei are strongly coupled across the entire embryo by wavefronts of metaphase and anaphase onset that travel at constant speed across the embryo. We summarize our observations as follows:

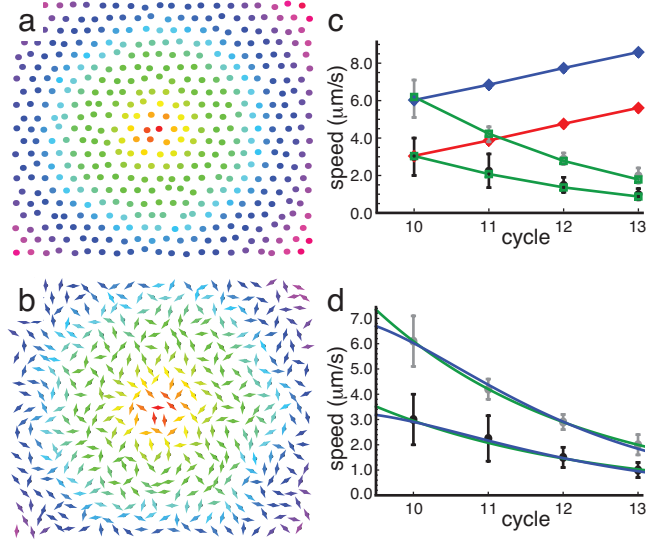


Figure 3. Two models for the propagation of wavefronts by chemical and mechanical signaling. a) Color plot showing the chemical wavefront in two dimensions. The wave starts in the center (red dot) with a single Dirac delta peak release. The color coding indicates when a nucleus releases its chemical to the bulk, going from red through the different hues of the rainbow to violet. b) Color plot showing the mechanical wavefront in two dimensions, including the orientations of the dipoles, which are picked at random. The color coding is the same as in figure a. c) Plot comparing the different results of the two models to the two sets of experimental data (black and gray dots with error bars). Blue diamonds: biochemical model with fixed time delay of 6 seconds. Red diamonds: biochemical model with fixed time delay of 10 seconds. Green squares: mechanical model with $D = \mu/\Gamma \sim 2^{-\gamma(n-n_0)}$ for $\gamma = 1.4$ and $\alpha = 0.1 \cdot Q$. d) Fits of the scaling forms of the mechanical model (green and blue curves) to the experimental data (black and gray dots with error bars). Green lines: fit to $v = v_0 \cdot 2^{(\beta-\gamma)(n-n_0)}$ for the case where $\bar{\alpha}$ is constant. Fit parameter $\gamma = 1.0$. Blue lines: fit to $v = v_0 \cdot 2^{(\beta-\gamma)(n-n_0)} g(\alpha \cdot 2^{2\beta(n-n_0)}, \nu)$ where $g(\bar{\alpha}, \nu) = -4(1 - \bar{\alpha}) \log(\bar{\alpha}) / (1 - \nu)$, and the absolute threshold α is fixed. Fit parameters: $\alpha = 0.1Q$, $\gamma = 1.4$.

1. There are at least two wavefronts in each cycle, corresponding to metaphase and anaphase, which travel at the same speed (figure 2b).
2. The common speed of the metaphasic and anaphasic wavefronts slows down exponentially in each successive cycle (figures 2c and 2e).
3. The metaphasic and anaphasic wavefronts are separated by the same time interval in each cycle for a given embryo (figure 2d).

In addition to these observations, we add those of Parry et al. [20]:

4. There is a calcium wavefront that coincides with the onset of anaphase.
5. The speed of the calcium wavefront slows down in each successive cycle, matching the speed of the anaphasic wavefront.

We now consider some scenarios to assess whether they are consistent with these observations. We note at the outset that the fact that the metaphasic and anaphasic wavefronts propagate with the same

speed, separated by a constant time interval, implies that there is a biochemical clock that sets the time interval.

Scenario A

A chemical wavefront triggers the metaphasic, calcium and anaphasic wavefronts. Here, we assume that there are clocks that cause both metaphase and anaphase to occur at specific time intervals after the biochemical signal triggers the clocks. In this case (4) implies that calcium cannot be the signal carrier, leaving the question what the signaling chemical is. Moreover, in this case, the results of the biochemical-signaling model suggest that (2) is very unlikely, since the model predicts that the speed of the wavefront should go up with cycle. Thus, Scenario A appears unlikely.

Scenario B

A mechanical wavefront triggers the metaphasic, calcium and anaphasic wavefronts. In this scenario, there is a mechanical wavefront that precedes the metaphasic wavefront. The stress released to maintain the mechanical wavefront starts a clock which triggers the onset of metaphase, calcium release and the onset of anaphase. Because the wavefront is mechanical, the wavefront speed slows down with cycle, according to the predictions of our mechanical signaling model. However, it is unclear what stress release triggers this wavefront, and how stress is released to amplify the signal to maintain the wavefront speed.

Scenario C

The metaphasic wavefront mechanically triggers the calcium and anaphasic wavefronts. In this scenario, the onset of metaphase itself at a nucleus leads to stress release. The stress starts a clock which triggers the release of calcium and also triggers the onset of anaphase. As a result, all three wavefronts travel at the same speed; because the metaphasic wavefront propagates mechanically, this speed slows down with successive cycles. In addition, the clock leads to fixed time intervals between the three wavefronts. This scenario is therefore consistent with all five observations. The scenario is also consistent with the expectation that the entire process of mitosis can be described by an extended wavefront, with metaphase, calcium release and anaphase as markers of this process that then also manifest as wavefronts.

Scenario C is consistent as well with independent observations made in *Xenopus* embryos. These embryos are not syncytial; instead they are divided into cells from the first cycle. It is unlikely that a biochemical signal could cross cell membranes to propagate a wavefront. Nevertheless, these embryos do exhibit metachronous mitosis [4]. They also exhibit calcium oscillations *inside* each cell, which precede anaphase [47]. Their behavior is therefore most consistent with Scenario C: the metaphasic mechanical wavefront triggers a calcium signal inside each cell and an anaphasic wavefront.

Scenario C implies several predictions. First, the metaphasic wavefront should precede the calcium wavefront, which precedes the anaphasic wavefront. Second, the speed of the calcium wavefront should be the same as the speed of the metaphasic and anaphasic wavefronts. Third, the time interval between the metaphasic and calcium wavefronts should be the same for all cycles for a given embryo. All of these predictions are consistent with the observations reported by Parry et al. [20], and can be further tested experimentally by combining labeled histones, as in our experiment, and calcium green dextran, as in the experiment of Parry et al. [20].

In principle, the estimated elastic constants and damping coefficients could be obtained directly from experiments by measuring the storage and loss moduli of the embryo surface *in vivo* using two-point microrheology. Optical tweezer experiments similar to the ones done by Schötz et al. [29] could also be used to extract the elastic moduli and the drag coefficient we used in our mechanical model. The actin concentration could be measured at the same time by staining the actin filaments with e.g. rhodamine, as done by Parry et al. [20] or GFP-moesin, as done by Cao et al. [48].

The key assumption in Scenario C is that the initial metaphasic wavefront also *propagates* mechanically. This can be tested by mechanically poking the embryo at different times within the cell cycle. If the cell is poked just in advance of the metaphasic wavefront, the poking itself should generate a wave that propagates from the poking site with the same speed as the metaphasic wavefront. In addition, this poking wavefront should stimulate the release of calcium. One would therefore expect that metaphasic, calcium and anaphasic wavefronts could be generated by poking the embryo mechanically. If the embryo is poked too far in advance of the metaphasic wave, there should be no response because the DNA in the nuclei has not yet been fully duplicated, so mitosis is not yet possible. If the embryo is poked after the metaphasic wavefront begins, there may be no response because calcium would already be depleted by the metaphasic wavefront. Thus, we would expect that poking could generate an anaphasic wavefront only if it is applied in a certain time window of the cycle. Another method to test the mechanical-signaling model is to destroy the filaments that mechanically couple the nuclei, which should prevent the mechanical wavefronts from propagating and thus the nuclei from synchronizing their mitosis. This could be done by injecting colcemid to disrupt the microtubules or latrunculin which affects actin filaments [3]. Other means of disrupting cytoskeletal filaments, via mutation or laser ablation, should also affect the mechanical wave.

4 Materials and Methods

4.1 Confocal videos

The imaged flies were from a His-GFP stock with a P[w+ ubi-H2A-GFP] insertion on the third chromosome. All embryos were collected at 25°C and dechorionated in 100% bleach for 1 minute. They were picked using a 70 μ m nylon strainer (BD Falcon), rinsed in distilled water and laid down on a semipermeable membrane (Biofolie). The excess water was absorbed and the embryos were immersed in Halocarbon oil 27 (Sigma Aldrich) and covered with a 22 \times 22 μ m coverslip (Corning). Embryos were imaged with a 20 \times oil immersion objective plan apochromat (Leica, NA=0.7) on a Leica SP5 laser scanning microscope with excitation wavelength of 488nm (argon laser 60mW). 8 bit images were taken every second at 512 \times 1024 0.45nm pixels and 1.4 μ s/pixel (734ms/image). An example video is shown in SI movie 1, available online [34].

4.2 Image analysis

We visualized nuclear DNA/chromosomes by tagging their histones with GFP. To determine the positions, sizes, aspect ratios and orientations of the DNA/chromosomes from each video frame, we developed a new image analysis technique, explained in detail in [49]. In brief, we first applied a bandpass filter to eliminate high-frequency noise. We then made a contour plot of the resulting image, found the locally highest-level contour (i.e., the contours with no other contour inside them), and identified each of them as a single nucleus. For each nucleus, we fit the contour at half-height with an ellipse to get its position, shape and orientation. An example of an experimental image with the chromosomal tracking overlaid is given in figure 1a.

Because the images were taken at high frequency (typically 1 Hz), the nuclei move less than their own radius from one frame to the next, simplifying tracking. The obvious exception is when nuclei divide during anaphase, and the observed shape splits in two. Because we detect shapes as well as positions of the chromosomes in each nucleus, tracking divisions is easy as well: when a nucleus divides, the chromosomes become highly elongated just before they split, and produce two almost circular daughters close to the endpoints of the long axis of the mother immediately after it splits, which are easily identified.

Acknowledgments

We thank Thomas Gregor for providing resources for the experiments and for his careful reading of the manuscript, and Xiaoyang Long for assistance with acquiring the experimental data. We also thank Gareth Alexander, Michael Lampson, and Tom Lubensky for helpful discussions. This work was partially supported by the Netherlands Organization for Scientific Research through a Rubicon grant (T.I.) and by NSF-DMR-1104637 (A.J.L.).

Appendices

A Embryo layout and replication cycle

The four main stages in the *Drosophila* embryo replication cycle, which we can detect from our movies, are illustrated in figure 4. A sketch of a cross-section of the embryo is shown in figure 5, illustrating how the nuclei are all located at the surface of the embryo for cycles 9-13 [1, 50].

Drosophila replication cycle

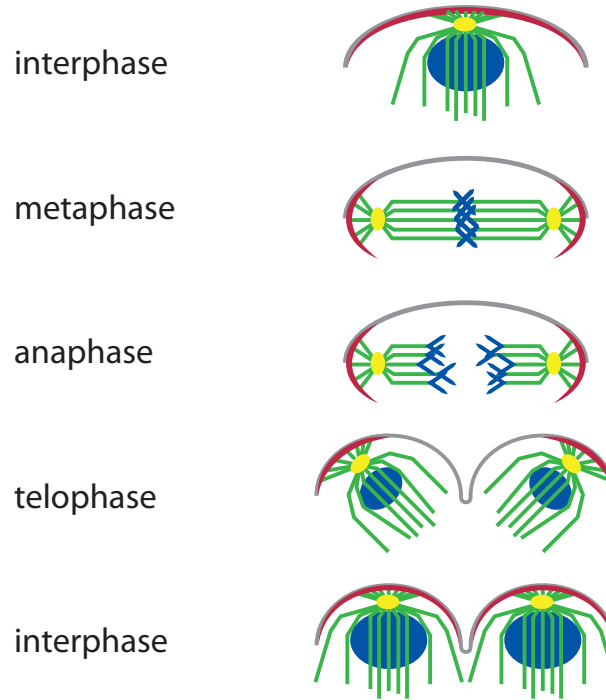


Figure 4. Illustration showing the four stages of the *Drosophila* embryo replication cycle that we can detect from our movies: interphase (DNA replication), metaphase (condensation of chromosomes in the nuclear midplane), anaphase (division of the nucleus in two daughter nuclei) and telophase (separation of daughter nuclei). The plasma membrane is shown in gray, the actin cap (made of actin filaments) in red, the microtubules in green, the centrosomes in yellow, and the DNA/chromosomes in blue.

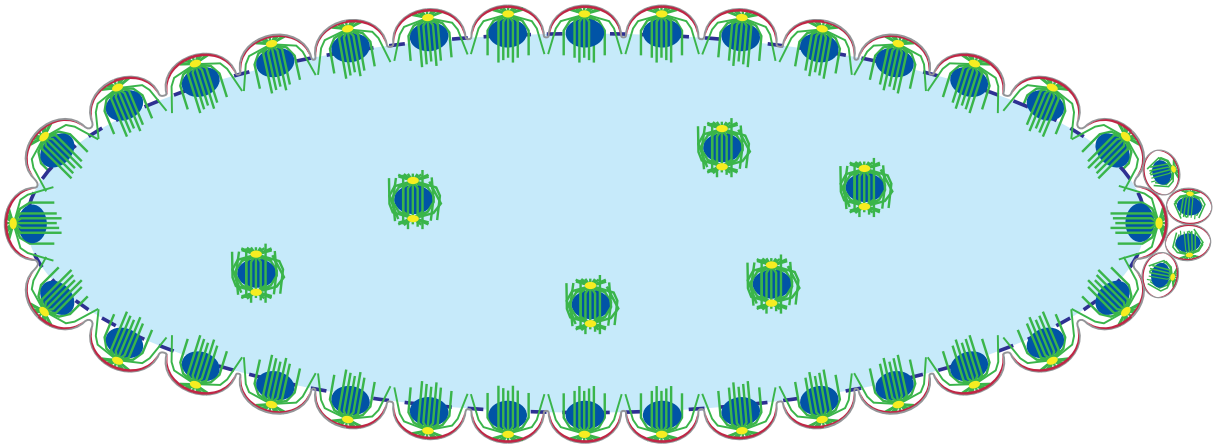


Figure 5. Sketch of a cross-section through a *Drosophila* embryo valid for stages 9-13. Most nuclei are located at the surface of the embryo. The nuclei are pushed outwards into the plasma membrane (gray), resulting in the formation of somatic buds. Each nucleus is enclosed in a microtubule basket (green) and contained in an individual actin cap (red), which gets disassembled after mitosis and re-assembled during interphase. DNA/chromosomes are shown in blue and centrosomes in yellow. The yolk (light blue) is a viscoelastic fluid containing water, cytoskeletal elements and necessary building blocks for the nuclei. The yolk is bounded by an actin cortex over which the nuclei can move. Also shown in this sketch are the small number of nuclei that reside inside the yolk, and the also small number of somatic cells that already form in cycle 10 at the posterior end (the pole cells that divide out of sync with the rest of the embryo). See Foe and Alberts [1] for sketches for each of the first 14 cycles and Schejter and Wieschaus [50] for a review on the cytoskeletal elements in the early embryo.

B Experimental data sets

Our image analysis results are for two different sets of experiments, which were carried out at ambient room temperature several months apart. The ambient temperature was higher for the second set, resulting in faster embryo development. We only used the data from those embryos which we could track from cycle 10-14 in the first set (Dataset 1, 3 embryos) and cycle 11-14 in the second set (Dataset 2, 4 embryos). SI movie 1 (available online [34]) is the raw data of one of the embryos from set 1. This confocal microscopy imaging movie shows a developing *Drosophila* embryo. The chromosomal histones are visualized by labeling with GFP. The version of the movie shown here shows 1 image per 15s, displayed at 5fps, so sped up 75x. Movies for data analysis were recorded at 1fps. The dimensions of each frame are $346 \times 440 \mu\text{m}$.

C Additional image analysis results

The average data from the two sets are given in table 1, and their average speeds are plotted on a log-linear scale in figure 6. The data from set 1 are given as closed symbols (blue, purple and green) in figure 2, the data from set 2 as open symbols (cyan, orange, gold and red). In figure 3c and d, and figure 6, the black dots correspond to the mean wavefront speeds of set 1, and the gray ones to the mean speeds of set 2.

In addition to the data shown in figure 2, we also measured the duration of each of the cycles (figure 7a). The numbers we found are consistent with those reported by Foe and Alberts [1] and Parry et al. [20]. Averaging over the embryos in each set, we find that the cycle duration can be reasonably approximated by a quadratic dependence on the cycle number (figure 7b).

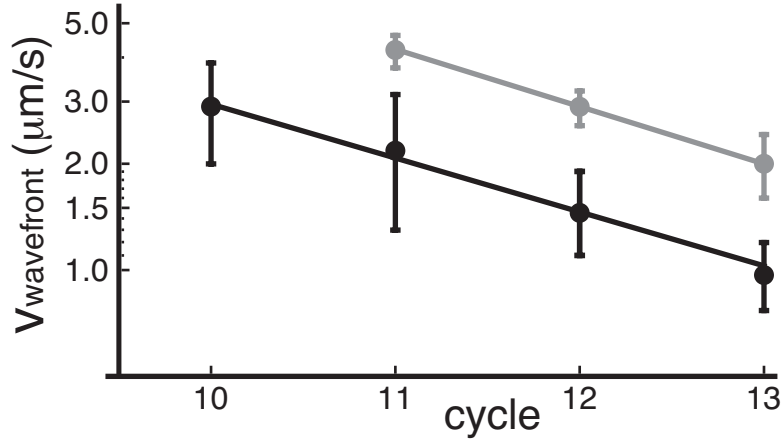


Figure 6. Average speed of each of the two sets of data, on a log-linear plot, fitted by an exponential $v \sim 2^{-\varepsilon(n-n_0)}$, $\varepsilon = 0.5 \pm 0.05$. The black dots correspond to the mean wavefront speeds of set 1, and the gray ones to the mean speeds of set 2.

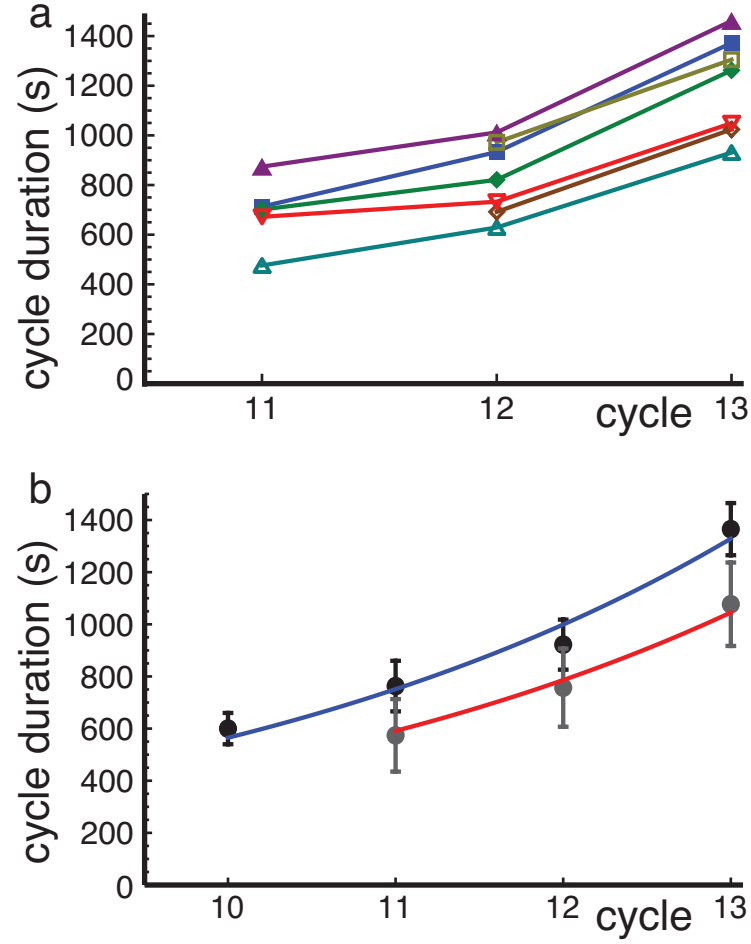


Figure 7. Duration of the measured cycles. a) Experimental data. The different symbols and colors correspond to the ones in figure 2. b) Cycle duration averaged over all experimentally observed embryos (black and gray dots for sets 1 and 2 respectively). The cycle durations can be fitted reasonably well by a weak exponential $t_n = t_0 e^{0.29 \cdot n}$, where $t_0 = 33\text{s}$ (set 1) and $t_0 = 25\text{s}$ (set 2).

D Exponential gradient model

In this section we investigate the ‘exponential gradient timing model’ for *Drosophila* embryo nuclear divisions. The idea behind this model is that the nuclei do *not* signal each other in any way that it is time to start mitosis; instead, they sample their local environment for a given protein, such as Bicoid (Bcd), and have the length of their cycle depend on the local concentration. Because the concentration of many such proteins does indeed exhibit a gradient from one of the two poles, this could explain how mitosis starts close to the poles, and then seems to ‘travel’ along the embryo, where in reality there is no traveling front at all.

Roughly speaking, there are four kinds of patterns expressed by proteins in the early *Drosophila* embryo: an exponential profile along the AP axis starting from one of the poles (of which Bcd is an example [35, 36]), an exponential profile along the DV axis (such as Dorsal [51]), a terminal morphogen profile which is high at both poles and both low and flat in between (as for the phosphorelation gradient of MAPK [51]), and a striped pattern (for e.g. Hunchback, Giant, Paired and Runt [37]). Because the observed mitotic waves start at the poles and then spread along the AP axis of the embryo, the striped patterns and the DV-axis gradients cannot be the ones causing them. There are often *two* mitotic waves, which start at the two opposite poles, which suggest that the terminal morphogens might be good candidates, but they hardly show any profile in the mid-60% of the embryo [51]. The most likely candidates are therefore the proteins that have an exponential profile along the AP axis, although in this case there must be at least two proteins that can trigger mitosis. This latter observation is a first weak point of the model discussed here, but not necessarily cause to rule it out.

During interphase, the nuclei in the syncytial embryo are surrounded by a nuclear membrane (also known as the nuclear envelope). One of the things the nucleus can do is to concentrate proteins inside that membrane. This has been observed directly for Bcd by Gregor et al. [36] and confirmed by our own observations. Irrespective of whether the proteins are concentrated in the nuclei during interphase, or they are distributed throughout the entire cytosol, they always exhibit an exponential decay along the anterior-posterior axis. As observed by Gregor et al. [36], the total amount of Bcd steadily increases over time, as more of the protein is translated in each cycle. In particular, the amount of protein keeps steady pace with the number of nuclei, such that at the start of each cycle, the actual amount of protein in each nucleus at a given position in the embryo is always the same [36].

Let us denote the position along the long axis by x , and the total length of the axis by L . The local concentration at x is then given by $c(x) = c_0 e^{-x/\lambda}$, where λ is the characteristic length scale of the exponential profile. As stated above, the experimental results of Gregor et al. tell us that λ is the same in all cycles, whereas c_0 goes up [36]. Assuming that all nuclei are equally good at collecting material from their environment, the amount of material collected by a single nucleus in a simple one-dimensional model of the embryo is given by

$$C(x, N) = \int_{x-L/2N}^{x+L/2N} c(y) dy = 2c_0\lambda \sinh\left(\frac{L}{2N\lambda}\right) e^{-x/\lambda}, \quad (4)$$

where N is the number of nuclei. As stated above, the key assumption of the model discussed here is that the duration of the cycle of each nucleus depends somehow on the concentration, or rather, on the amount of material in the nucleus, so we have

$$\Delta t_{\text{cycle}} = f(C(x, N)) = f\left(2c_0\lambda \sinh\left(\frac{L}{2N\lambda}\right) e^{-x/\lambda}\right). \quad (5)$$

Unfortunately, we do not know what the function f in equation (5) is. The only thing we do know is that it is monotonously increasing with its argument (the total amount of material in a nucleus). We will therefore explore two explicit possibilities:

- The simplest possible dependence: f is a linear function.

- The dependence that gives the observed behavior of (effective) wavefronts, i.e., that the resulting ‘speed’ v of mitosis events through the embryo is well-defined and constant throughout, and $\Delta t_{\text{cycle}} = x/v$.

For the first option, we write $f(\alpha) = t_0 - \tau\alpha$, with t_0 some offset time and τ a timescale. We can then calculate the speed of an observed mitotic wavefront, as a function of the number of nuclei N , by calculating the time difference between two positions x and y in the embryo:

$$\begin{aligned} v(x, y, N) &= \frac{y - x}{\Delta t_{\text{cycle}}(y, N) - \Delta t_{\text{cycle}}(x, N)} \\ &= \frac{y - x}{2c_0\lambda\tau \sinh\left(\frac{L}{2N\lambda}\right) (e^{-x/\lambda} - e^{-y/\lambda})}. \end{aligned} \quad (6)$$

Equation (6) shows that v depends on the position, so there is no well-defined wavespeed in this model. This is of course no big surprise - we just took a random functional dependence for f , so there should be no reason to expect it would produce a wavespeed that is position-independent. However, this does illustrate the point that a constant wavespeed is something special: we need to specifically *choose* f such that a constant speed comes out.

Note that it may of course be that there is no constant wavespeed, but that it only appears to be constant within our error bars. Although we can not rule this option out, this also does not come out naturally. For instance, inserting numbers for *Drosophila* from Gregor et al. [37] ($L = 450\mu\text{m}$, $\lambda = 70\mu\text{m} = 0.15L$, $N = 50$) we find that for $x = 0$, the measured speed more than doubles as we take the measuring point y across the embryo, which can certainly not be confused with a constant speed.

To get a constant speed, we need to choose a different function f , specifically a logarithm: $f(\alpha) = t_0 + \tau \log \alpha$. In this case we find:

$$v(x, y, N) = \frac{y - x}{(\tau/\lambda)(y - x)} = \lambda/\tau. \quad (7)$$

In this case, we do indeed find a constant value of v across the embryo. However, we also find that v is independent of N . v does depend on the decay length λ , but the value of λ does not change [36]. The wavefront speed predicted by this model is therefore the same for all cycles, in direct contradiction to what we observe.

E Diffusion model

The process of diffusion is governed by the diffusion equation, here given for a concentration field $c(\vec{x}, t)$:

$$\frac{\partial c(\vec{x}, t)}{\partial t} = D\nabla^2 c(\vec{x}, t), \quad (8)$$

where D is the diffusion constant. Equation (8) is linear, so we can use the superposition principle: the sum of any two solutions is itself a solution. The general solution for a system with no boundaries depends only on the initial condition $c(\vec{x}, 0)$, and is given by

$$c(\vec{x}, t) = \int G(\vec{x}, \vec{y}, t) c(\vec{y}, 0) d\vec{y}, \quad (9)$$

where $G(\vec{x}, \vec{y}, t)$ is the Green’s function of the diffusion equation, which for a system in n dimensions is given by

$$G(\vec{x}, \vec{y}, t) = \frac{1}{(4\pi Dt)^{n/2}} \exp\left(-\frac{|\vec{x} - \vec{y}|^2}{4Dt}\right). \quad (10)$$

The Green’s function describes the concentration field at \vec{x} at time t due to a single delta-function concentration source at \vec{y} at time 0.

F Mechanical model

As described in the main text above, we can describe the medium in which the nuclei live as an overdamped elastic medium. Motion in this medium can be described by some displacement vector \vec{u} from a fixed reference position. We get force balance by equating the damping forces acting on the nuclei (due to friction with the cortical actin layer surrounding the yolk or the outer membrane, and drag due to the viscous fluids the nuclei and their surrounding microtubule baskets are immersed in) to the elastic forces in the polymer cytoskeleton:

$$\Gamma \partial_t u_i = \frac{E}{2(1+\nu)} \partial_j \partial_j u_i + \frac{E}{2(1-\nu)} \partial_i \partial_j u_j. \quad (11)$$

As also pointed out above, equation (11) is reminiscent of the diffusion equation: a time derivative on the left equals second-order space derivatives plus a source term on the right, and it comes as no surprise that the solution depends on a quantity with the dimension of a diffusion constant $D = \mu/\Gamma$, where μ is the material's shear modulus and equals $E/(2+2\nu)$. Moreover, equation (11) also allows for a Green's function type solution, but here in the form of a tensor $G_{ijk}(\vec{x}, t)$, relating an arbitrary input $Q_{ij}\delta(\vec{x})\Theta(t)$ to a resulting displacement vector $u_k(\vec{x}, t)$ [32]. In two dimensions, the input tensor Q_{ij} has three independent components, and can be decomposed in a (hydrostatic) expansion/contraction, a torque and a force dipole. The dividing nuclei in the *Drosophila* system can be well described by the force dipole, with the mitotic spindles pulling the nuclei apart generating the forces, while the volume remains fixed and there is no rotation. An example displacement field due to a single force dipole at the origin is given in figure 8.

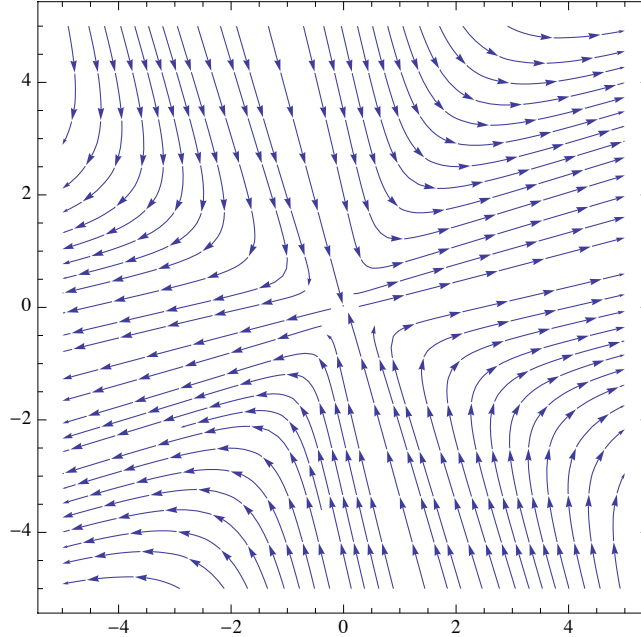


Figure 8. Example of a displacement field due to a single force dipole located at the origin and having an angle of $\pi/6$ with respect to the x -axis, obtained by taking the $t \rightarrow \infty$ limit of $G_{ijk}(\vec{x}, t)Q_{ij}$.

G Wavefronts

Now that we know the solutions to the chemical and mechanical diffusion equations due to a single source, we can exploit the fact that the chemical and stress diffusion equations (8 and 11) are linear to compute the behavior of a system with many sources using the superposition principle. For simplicity, we pre-arrange the nuclei on a triangular grid, with a little noise in the position of each nucleus to prevent artifacts due to a perfect arrangement. This is consistent with our observation that just before the mitosis waves the nuclei in an actual embryo have a rather high degree of triangular order, except where there are defects due to the fact that a nucleus did not divide in an earlier cycle. Alternatively, we can also consider packings with short-range correlations but no long-range order (like the packing of soft repulsive spheres), which gives the same results [32].

G.1 Wavefronts in the biochemical diffusion model

We will describe the release by a nucleus of a biochemical with a Dirac delta function source located at the position of the nucleus. Because integration is a linear operation, adding two sources, even if they divide at different times, is trivial - we simply carry out the integration in equation (9) for each nucleus that has already divided with the time properly offset, then sum over these nuclei. The only problem is to determine when each nucleus is supposed to divide. To find out, we perform what is essentially a numerical integration over time. We start with a release of material at the origin, which we model by having a delta function concentration there at $t = 0$. By construction, the concentration field is then given by $G(\vec{x}, 0, t)$ as long as no other sources have released their chemicals into the system. We proceed in small timesteps Δt , calculating for each timestep the concentration at the location of each of the nuclei that have not yet divided, given the total concentration field generated by the nuclei that have divided so far. Suppose there is a total number of N nuclei, M of which have already released their chemicals. The i th source is located at $\vec{x} = \vec{a}_i$, released its chemicals at $t = t_i$, and the t_i 's are ordered. For $t_M < t < t_{M+1}$ we then find by using the superposition principle:

$$c(\vec{x}, t) = \sum_{i=1}^M \frac{1}{4\pi D(t - t_i)} \exp\left(-\frac{|\vec{x} - \vec{a}_i|^2}{4Dt}\right), \quad (12)$$

where we have taken $n = 2$. From $c(\vec{x}, t)$ we can determine when the next source will release its chemicals, by solving $c(\vec{a}_j, t) = \alpha$ for $M + 1 \leq j \leq N$. We thus check all nuclei that have not yet released anything, and determine which one will be the next source by finding the one with the smallest value of t , which sets t_{M+1} . If there is a nonzero delay time between activation and release, we simply add it to the found value of t_{M+1} . Given the positions of the sources, the system thus has three parameters: the diffusion constant D , the release concentration α , and the delay time t_{delay} . The ‘release-wave’ is then the time at which a given source releases its chemicals versus its distance to the origin (i.e., the first source). An example is given in figure 3a, which reveals a clear wavefront with a well-defined wave speed. Figure 9 shows the effect of adding delay times: after an initial transit due to finite-size effects near the origin, there is again a well-defined wave speed, which slows down with increasing t_{delay} , and also becomes less dependent on the source density as t_{delay} goes up.

G.1.1 Algorithm for finding wavefronts

In summary, we use the following algorithm to numerically find the wavefronts within the biochemical diffusion model (and, with the proper adaptations, for the stress diffusion model as well):

- Generate a grid of hexagonally arranged nuclei with some small positional noise, centered at the origin.

- Start with a delta function concentration at the origin at $t = 0$.
- Increase time in steps of Δt . For each timestep, calculate the local concentration at each of the sites of the nuclei, due to the nuclei that have released chemical so far. If one of these exceeds the critical concentration α , add a delta function concentration peak at this location and time.
- Stop after either all nuclei have divided or a predefined time has been reached.

G.1.2 Analysis of the steady-state wavefront

In the case without delay time, it is fairly easy to determine the speed of the wavefront for the regime in which the wavefront is well-established, i.e., when its curvature is small. Suppose the lattice spacing is a , and the time it takes to get from one row to the next is t . The speed, in a triangular lattice, is then $v = a * \frac{1}{2}\sqrt{3}/t$, because the spacing between the two layers is $a * \frac{1}{2}\sqrt{3}$. To find the time, it turns out to be sufficient to only consider the 2 nearest neighbors in the previous row. We choose coordinates such that the neighbors are located at $(\pm \frac{a}{2}, 0)$, and our next nucleus is at $(0, \frac{a}{2}\sqrt{3})$. Then the time at which this next nucleus is activated is given by the solution of

$$\alpha = \frac{2}{4\pi Dt} \exp \left[-\frac{a^2}{4Dt} \right]. \quad (13)$$

The results obtained using equation (13) are almost identical to those obtained by numerical solution of the full equations. Corrections can of course be made by including additional sources, but in this case that is not necessary.

To analyze equation (13) further, we introduce dimensionless variables $\bar{\alpha} = 4\pi a^2 \alpha$ and $\tau = Dt/a^2$. The equation then becomes

$$\bar{\alpha} = \frac{2}{\tau} e^{-1/4\tau}, \quad (14)$$

which can of course not be solved analytically, but is easy to solve numerically. We note that the right hand side of (14) has a maximum value of $\bar{\alpha}_{\max} = 8/e$ at $\tau = 1/4$, giving the condition that there can only be a wave if $\alpha < 2/\pi e a^2$. If we write the inverse of (14) as $\tau = f(\bar{\alpha})$, we can write for the wavefront speed

$$v = \frac{D}{a} \frac{1}{2} \sqrt{3} \frac{1}{f(\bar{\alpha})}, \quad (15)$$

so $v \propto D$ if both a and α are fixed, but unfortunately the scaling of the speed with a and α is hidden in $f(\bar{\alpha})$. Based on the numerical determination of $f(\bar{\alpha})$ we can capture its features fairly accurately with the following function

$$f(\bar{\alpha}) \approx b_1 \bar{\alpha}^{1/n} \left[\frac{1}{4} - b_2 \left(\frac{8}{e} - \bar{\alpha} \right)^{1/m} \right], \quad (16)$$

where fitting gives $b_1 = 0.93$, $b_2 = 0.14$, $n = 6.6$ and $m = 3.6$ (see figure 11). Our numerical solutions of the full equations show that the data do indeed collapse onto the curve described by equations (15) and (16) for different diffusion coefficients and nuclear spacings (figure 12). In particular, we find that the wavefront speed v always *increases* as the nuclear spacing a *decreases*, so v increases with increasing cycle number.

G.2 Wavefronts in the biochemical diffusion model with delay time

As indicated in Section G.1, we can include a delay time t_{delay} into our diffusion model. Now a nucleus divides (i.e., releases its chemicals) a time t_{delay} *after* the local concentration first reaches the threshold value α . For small delay times, this will simply slow down the wavefront speed a little. However, for

even moderately larger delay times, this has severe consequences, because the chemicals released earlier will continue to travel outward, pushing the next line closer to the threshold value, possibly even over it. We will therefore not be able to suffice with as simple a calculation as before, where the only two sources that mattered were the nearest neighbors in the previous row. Instead, we need to include many previous rows. Fortunately, the nearest-neighbor approximation still holds: a source is to very good approximation only influenced by its nearest neighbors in the previous row, plus their nearest neighbors in the row before that, and so on. That means that for each source we have a wedge-shape region of older sources that can influence it: 2 in the previous row, 3 in the row before, etc.

We assume we have reached steady-state, and the wavefront is moving with a constant speed v from one horizontal row to the next. The distance between the rows is still $\frac{1}{2}a\sqrt{3}$, and the time it takes the front to cover this distance is Δt . As before, we nondimensionalize, defining $\bar{\alpha} = 4\pi a^2 \alpha$, $\tau = D\Delta t/a^2$, and $\tau_d = Dt_{\text{delay}}/a^2$. The local concentration in dimensionless parameters at the location of the next source is then given by

$$\bar{c}(\tau, \tau_d) = \sum_{n=n_0}^{n_{\text{max}}} \bar{c}_n(\tau, \tau_d), \quad (17)$$

$$\bar{c}_n(\tau, \tau_d) = \frac{1}{n\tau - \tau_d} \sum_{m=-n/2}^{n/2} \exp\left[-\frac{\frac{3}{4}n^2 + m^2}{4(n\tau - \tau_d)}\right]. \quad (18)$$

In equation (18), we sum over all the relevant sources in row n , which were all activated a nondimensionalized time $n\tau - \tau_d$ ago. In equation (17) we sum over the relevant rows: starting at n_0 , the last row that was activated, up to either a large enough value n_{max} (for true steady-state) or the actual value if we want to account for finite-size effects. To determine n_0 , we note that \bar{c}_n is not defined for $\tau < \tau_d/n$, therefore n_0 is given by the smallest value of n_0 such that

$$\bar{\alpha} > \lim_{\tau \downarrow \tau_d/n_0} \bar{c}(\tau, \tau_d, n_0) \quad (19)$$

is satisfied. Figure 13 shows $\bar{c}(\tau, \tau_d)$ for two values of τ_d , showing how different values of τ correspond to different values of n_0 . The function $\bar{c}(\tau, \tau_d)$ is a smooth function of τ , but for large enough values of τ_d , it is not monotonous, unlike the relation between $\bar{\alpha}$ and τ for the case without delay time (figure 11). The inverse of \bar{c} will therefore not be continuous for τ_d larger than some critical value, which also means that the resulting wavefront speed is no longer a continuous function of the threshold concentration $\bar{\alpha}$ (figure 14).

G.2.1 Fitting the data with time delay

Naturally, the more parameters we have, the easier it is to fit any set of experimental data points. In the diffusion model with delay time we have four parameters: the diffusion constant D , the grid size a , the threshold value α and the delay time t_{delay} . The grid size (i.e. the spacing between the nuclei) is measured independently, leaving us with three parameters which we can vary. Reasonable values for the diffusion constant for a small chemical in the early *Drosophila* embryo are $D = 5 - 100 \mu\text{m}^2/\text{s}$, as measured by Gregor et al. [37]. As indicated in the main text above, we cannot fit the experimental trend (a wavefront speed that decreases exponentially with cycle number) with fixed values for t_{delay} and α for any value of D within this range (see figure 3c). The only way we can thus fit the experimental data within this model is if either (or both) of α and t_{delay} change with the cycle number.

We have systematically investigated a number of options, changing α or t_{delay} with cycle number. Some results are given in table 2. We did not find any result that fit the data in which the numbers change in a well-defined way (e.g. the delay time increasing linearly or exponentially with the cycle number). Moreover, in the case of variable delay time, we find that in the first cycle (cycle 10), the

interaction is between nearest-neighbors as in the model without time delay, but the interaction range goes up every cycle, up to 5 rows apart in cycle 13. In the case of variable concentration threshold, we need a change of at least an order of magnitude in each cycle to fit the experimental data. Even in the case where we allow both variables to change, we keep finding at least one of these two problems. Even though we cannot strictly rule out the diffusion model with variable time delay and concentration threshold, these results make it very unlikely that this model is actually correct.

G.3 Wavefronts in the mechanical model

The analysis leading to wavefront propagation in the mechanical model is described in Ref. [32]. As in the case of diffusion, we must set a threshold to determine when a source (a nucleus) is activated. The simplest option is to look at the eigenvalues of the stress tensor: if the largest of those (taking absolute values) exceeds a certain threshold α , the nucleus is activated. An activated nucleus adds an additional force dipole term to the stress field in the system, which in turn of course affects the displacement field, as described by the Green tensor solution of equation (11). Note that we assume linear elasticity, so that the strain is linear in the displacement, and the stress is linear in the strain. The superposition principle therefore holds not just for the displacements but for the strain and stress fields as well.

We let each nucleus divide (i.e. generate a force dipole) along a random orientation. The implementation of the stress-mediated signaling model follows the same pattern as that of the chemical-diffusion-mediated signaling model, with the concentration c replaced by the stress tensor σ_{ij} . An example implementation on a grid of 21×21 nuclei is shown in figure 15. The figure shows a clear wavefront which has a well-defined speed.

As in the diffusion model, we analyze our mechanical model in terms of dimensionless parameters. There is only one quantity in our model that has the dimensions of a speed, namely $\mu/a\Gamma$, which means that the resulting wavefront speed has to scale linearly with this factor, as indeed it does. We define a dimensionless wavefront speed $\bar{v} = \frac{a\Gamma}{\mu}v$ and a dimensionless stress threshold $\bar{\alpha} = a^2\alpha/Q$, where Q is the strength of the force dipole. We can then write

$$v = \frac{\mu}{a\Gamma}g(\bar{\alpha}, \nu) \quad (20)$$

We determine the function $g(\bar{\alpha}, \nu)$ by numerically solving the model. The best numerical fit to the experimental data is shown in figure 2c. As detailed in [32], we find that it can be well described by the following functional form, derived using a similar argument we used to arrive at equation (14) for the diffusion model:

$$g(\bar{\alpha}, \nu) = -\frac{4(\bar{\alpha} - 1)\log(\bar{\alpha})}{1 - \nu}. \quad (21)$$

Note that the form in equation (21) differs slightly from that in [32] because of the use of the shear modulus μ instead of the Young's modulus E in the definition of \bar{v} . We use equations (20) and (21) to fit the experimental data in figure 2d.

Data set 1				
cycle number	10	11	12	13
nuclear spacing (μm)	23.4 ± 0.8	18.2 ± 0.6	13.2 ± 0.3	9.7 ± 0.2
wavefront speed ($\mu\text{m/s}$)	2.9 ± 0.9	2.2 ± 0.9	1.5 ± 0.4	1.0 ± 0.2
cycle duration (s)	600 ± 60	763 ± 97	922 ± 96	1365 ± 100
mitosis duration (s)	237 ± 8	231 ± 9	233 ± 12	240 ± 12

Data set 2			
cycle number	11	12	13
nuclear spacing (μm)	18.0 ± 1.2	13.5 ± 0.3	10.0 ± 0.4
wavefront speed ($\mu\text{m/s}$)	4.2 ± 0.4	2.9 ± 0.3	2.0 ± 0.4
cycle duration (s)	574 ± 139	757 ± 150	1077 ± 160
mitosis duration (s)	197 ± 32	194 ± 26	194 ± 24

Table 1. Experimental data averaged over the data sets. Data sets 1 and 2 correspond to two different sets of measurements, taken on different days. They correspond to respectively the closed and open symbols in figure 2 and figure 7a.

cycle number	nuclear spacing (μm)	wavefront speed ($\mu\text{m/s}$)	t_{delay} (s) (α fixed)	α ($10^{-4}/\mu\text{m}^2$) (t_{delay} fixed)	$(t_{\text{delay}}, \alpha)$ (s, $10^{-4}/\mu\text{m}^2$)
10	23.4 ± 0.8	2.9 ± 0.9	1.5	0.0044	(5, 0.254)
11	18.2 ± 0.6	2.2 ± 0.9	5.7	0.29	(10, 0.300)
12	13.2 ± 0.3	1.5 ± 0.4	16.0	6.9	(20, 0.685)
13	9.7 ± 0.2	1.0 ± 0.2	36.1	31	(40, 1.057)

Table 2. Experimentally determined values of the nuclear spacing and wavefront speed (set 1), and numerically determined values of the required delay time t_{delay} and threshold concentration α to fit the experimental data. In column four, $D = 15 \mu\text{m}^2/\text{s}$ and $\alpha = 5 \cdot 10^{-4} \mu\text{m}^{-2}$; in column 5, $D = 10 \mu\text{m}^2/\text{s}$ and $t_{\text{delay}} 10$ s; in column 6, $D = 10 \mu\text{m}^2/\text{s}$ and t_{delay} is assumed to double in each cycle. None of the columns show a systematic dependency of the parameters on the cycle number, making it impossible to assign predictive power to the numbers found, or to find a model to explain the dependencies. Note also that for the case of fixed delay time (column 5), we need to assume that the threshold value goes up by at least an order of magnitude in each cycle. In the case of variable delay time (columns 4 and 6), the interactions become very long-ranged in the later cycles, with nuclei up to 5 rows apart triggering each other in cycle 13, even though in cycle 10 the interaction only involves nearest neighbors.

References

1. Foe VE, Alberts BM (1983) Studies of nuclear and cytoplasmic behaviour during the five mitotic cycles that precede gastrulation in *Drosophila* embryogenesis. *J Cell Sci* 61: 31-70.
2. Foe VE (1989) Mitotic domains reveal early commitment of cells in *Drosophila* embryos. *Development* 107: 1-22.
3. Foe VE, Odell G, Edgar BA (1993) Mitosis and morphogenesis in the *Drosophila* embryo: Point and Counterpoint. In: Bate M, Martinez-Arias A, editors, *Development of Drosophila melanogaster*. Cold Spring Harbor: Cold Spring Harbor Press, pp. 149-300.
4. Satoh N (1977) Metachronous cleavage and initiation of gastrulation in amphibian embryos. *Development, Growth and Differ* 19: 111-117.
5. Newport J, Kirschner M (1982) A major developmental transition in early *Xenopus* embryos: I. Characterization and timing of cellular changes at the midblastula stage. *Cell* 30: 675-686.
6. Saka Y, Smith JC (2001) Spatial and temporal patterns of cell division during early *Xenopus* embryogenesis. *Dev Biol* 229: 307-318.
7. Kageyama T (1986) Mitotic wave in the yolk syncytial layer of embryos of *Oryzias latipes* originates in the amplification of mitotic desynchrony in early blastomeres. *Zool Sci* 3: 1046.
8. Trinkaus JP (1992) The midblastula transition, the YSL transition and the onset of gastrulation in *Fundulus*. *Development* 116: 75-80.
9. Kane DA, Warga RM, Kimmel CB (1991) Mitotic domains in the early embryo of the zebrafish. *Nature* 360: 735-737.
10. Kane DA, Kimmel CB (1993) The zebrafish midblastula transition. *Development* 119: 447-456.
11. Devreotes P (1989) *Dictyostelium discoideum*: a model system for cell-cell interactions in development. *Science* 245: 1054-1058.
12. Levine H, Reynolds W (1991) Streaming instability of aggregating slime mold amoebae. *Phys Rev Lett* 66: 2400-2403.
13. Lee KJ, Cox EC, Goldstein RE (1996) Competing patterns of signaling activity in *Dictyostelium Discoideum*. *Phys Rev Lett* 76: 1174-1177.
14. Kleckner N, Zickler D, Jones GH, Dekker J, Padmore R, et al. (2004) A mechanical basis for chromosome function. *Proc Natl Acad Sci USA* 101: 12592-12597.
15. Alberts B, Johnson A, Lewis J, Raff M, Roberts K, et al. (2008) *Molecular biology of the cell*. New York, NY, U.S.A.: Garland Science, 5th edition.
16. Silver RB (1989) Nuclear envelope breakdown and mitosis in sand dollar embryos is inhibited by microinjection of calcium buffers in a calcium-reversible fashion, and by antagonists of intracellular Ca²⁺ channels. *Dev Biol* 131: 11-26.
17. Silver RB (1990) Calcium and cellular clocks orchestrate cell division. *Ann N Y Acad Sci* 582: 207-221.
18. Thomas AP, Bird GSJ, Hajnóczky G, Robb-Gaspers LD, Putney JW (1996) Spatial and temporal aspects of cellular calcium signaling. *FASEB J* 10: 1505-1517.

19. Allbritton NL, Meyer T (1993) Localized calcium spikes and propagating calcium waves. *Cell Calcium* 14: 691-697.
20. Parry H, McDougall A, Whitaker M (2005) Microdomains bounded by endoplasmic reticulum segregate cell cycle calcium transients in syncytial *Drosophila* embryos. *J Cell Biol* 171: 47-59.
21. Parry H, McDougall A, Whitaker M (2006) Endoplasmic reticulum generates calcium signalling microdomains around the nucleus and spindle in syncytial *Drosophila* embryos. *Biochem Soc Trans* 34: 385-388.
22. Jaffe LF (2008) Calcium waves. *Phil Trans R Soc B* 363: 1311-1316.
23. Whitaker M (2008) Calcium signalling in early embryos. *Phil Trans R Soc B* 363: 1401-1418.
24. Warn RM, Magrath R, Webb S (1984) Distribution of f-actin during cleavage of the *Drosophila* syncytial blastoderm. *J Cell Biol* 98: 156-162.
25. Karr TL, Alberts BM (1986) Organization of the cytoskeleton in early *Drosophila* embryos. *J Cell Biol* 102: 1494-1509.
26. Sullivan W, Theurkauf WE (1995) The cytoskeleton and morphogenesis of the early *Drosophila* embryo. *Curr Opin Cell Biol* 7: 18-22.
27. Stevenson VA, Kramer J, Kuhn J, Theurkauf WE (2001) Centrosomes and the scrambled protein coordinate microtubule-independent actin reorganization. *Nat Cell Biol* 3: 68-75.
28. Kanesaki T, Edwards CM, Schwarz US, Grosshans J (2011) Dynamic ordering of nuclei in syncytial embryos: a quantitative analysis of the role of cytoskeletal networks. *Integr Biol* 3: 1112-1119.
29. Schötz EM (2004) In vivo manipulation of *Drosophila* syncytial blastoderm embryos using optical tweezers. Diploma thesis, Universität Konstanz, Konstanz, Germany.
30. Winfree AT (1972) Spiral waves of chemical activity. *Science* 175: 634-636.
31. Agladze KI, Krinsky VI (1982) Multi-armed vortices in an active chemical medium. *Nature* 296: 424-426.
32. Idema T, Liu AJ (2013) Mechanical signaling via nonlinear wavefront propagation in a mechanically-excitable medium. arXiv:1304.3657.
33. Majkut S, Idema T, Swift J, Krieger C, Liu AJ, Discher DE (2013) Heart-specific stiffening in early embryos parallels matrix and myosin expression to dynamically match cell function. *Curr Biol* (under review)
34. Supplementary confocal microscopy imaging movie of a developing *Drosophila* embryo available at <http://idemalab.tudelft.nl/research/drosophilamovie.html>.
35. Driever W, Nüsselein-Volhard C (1988) A gradient of *bicoid* protein in *Drosophila* embryos. *Cell* 54: 83-93.
36. Gregor T, Wieschaus EF, McGregor AP, Bialek W, Tank DW (2007) Stability and nuclear dynamics of the bicoid morphogen gradient. *Cell* 130: 141-152.
37. Gregor T, Bialek W, de Ruyter van Steveninck RR, Tank DW, Wieschaus EF (2005) Diffusion and scaling during early embryonic pattern formation. *Proc Natl Acad Sci USA* 102: 18403-18407.

38. Lang I, Scholz M, Peters R (1986) Molecular mobility and nucleocytoplasmic flux in hepatoma cells. *J Cell Biol* 102: 1183-1190.
39. Chaikin PM, Lubensky TC (1995) Principles of condensed matter physics. Cambridge, U.K.: Cambridge University Press.
40. Palmer A, Mason TG, Xu J, Kuo SC, Wirtz D (1999) Diffusing wave spectroscopy microrheology of actin filament networks. *Biophys J* 76: 1063-1071.
41. Müller O, Gaub HE, Bärmann M, Sackmann E (1991) Viscoelastic moduli of sterically and chemically cross-linked actin networks in the dilute to semidilute regime: measurements by oscillating disk rheometer. *Macromolecules* 24: 3111-3120.
42. Janmey PA, Hvidt S, Käs J, Lerche D, Maggs A, et al. (1994) The mechanical properties of actin gels. *J Biol Chem* 269: 32503-32513.
43. Gardel ML, Valentine MT, Crocker JC, Bausch AR, Weitz DA (2003) Microrheology of entangled F-actin solutions. *Phys Rev Lett* 91: 158302.
44. Gardel ML, Shin JH, MacKintosh FC, Mahadevan L, Matsudaira PA, et al. (2004) Scaling of F-actin network rheology to probe single filament elasticity and dynamics. *Phys Rev Lett* 93: 188102.
45. Doi M, Edwards SF (1986) The theory of polymer dynamics. Oxford, UK: Oxford University Press.
46. MacKintosh FC, Käs J, Janmey PA (1995) Elasticity of semiflexible biopolymer networks. *Phys Rev Lett* 75: 4425-4428.
47. Keating TJ, Cork RJ, Robinson KR (1994) Intracellular free calcium oscillations in normal and cleavage-blocked embryos and artificially activated eggs of *Xenopus laevis*. *J Cell Sci* 107: 2229-2237.
48. Cao J, Crest J, Fasulo B, Sullivan W (2010) Cortical actin dynamics facilitate early-stage centrosome separation. *Curr Biol* 20: 770 - 776.
49. Idema T (2012) A new way of tracking motion, shape and divisions. *Eur Biophys J* (under review).
50. Schejter ED, Wieschaus E (1993) Functional elements of the cytoskeleton in the early *Drosophila* embryo. *Annu Rev Cell Biol* 9: 67-99.
51. Sample C, Shvartsman SY (2010) Multiscale modeling of diffusion in the early *Drosophila* embryo. *Proc Natl Acad Sci USA* 107: 10092-10096.

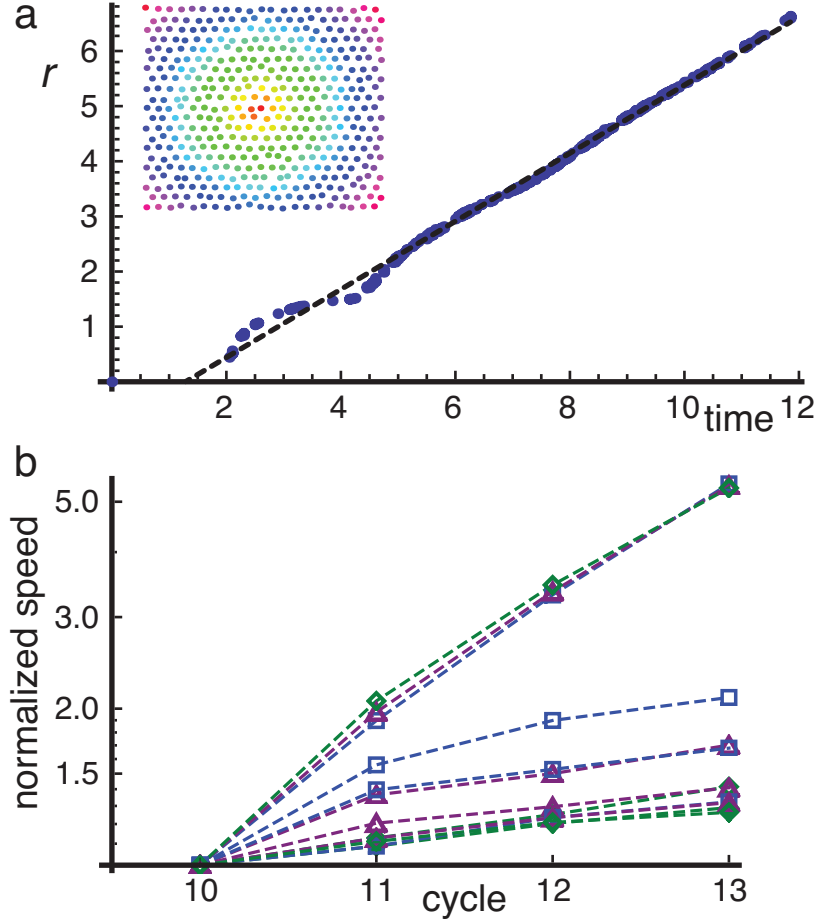


Figure 9. Wavefronts in the diffusion model with a time delay. a) Distance to center r vs. activation time t shown for a system in which there is a delay time between the local concentration reaching the threshold value α and the nucleus releasing new material to the bulk. After a characteristic transition regime the system once again exhibits a wave front. Inset: Wavefront visualized in two dimensions using a color plot. The wave starts in the center (red dot) with a single Dirac delta peak release. The color coding indicates when a nucleus releases its chemical to the bulk, going from red through the different hues of the rainbow to violet. b) Effect of the delay time on the wavefront speed for three different values of the diffusion constant (blue, purple, green). In a system without any time delay, the dynamics is dominated by diffusion, and can be collapsed by normalizing the speed with that of the largest grid size (top lines). For high delay times, the dynamics become independent of the diffusion and once again collapse (bottom lines). In between, the dynamics depend qualitatively on the exact parameters chosen.

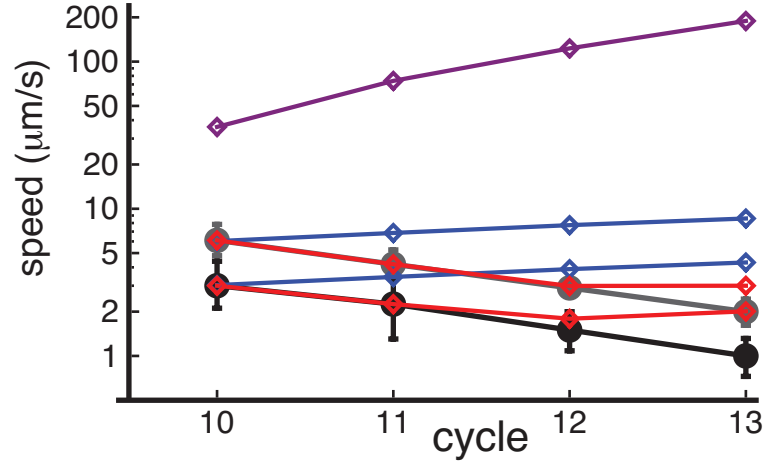


Figure 10. Plot comparing the results of the diffusion model to the experimental data (black (set 1) and gray (set 2) dots). Purple diamonds: diffusion model with fixed diffusion constant of $100 \mu\text{m}^2/\text{s}$ and no time delay. Blue diamonds: diffusion model with fixed time delay of 6 seconds (top set) and 10 seconds (bottom set). Red diamonds: best fits for the diffusion model with the time delay scaling exponentially with the cycle number.

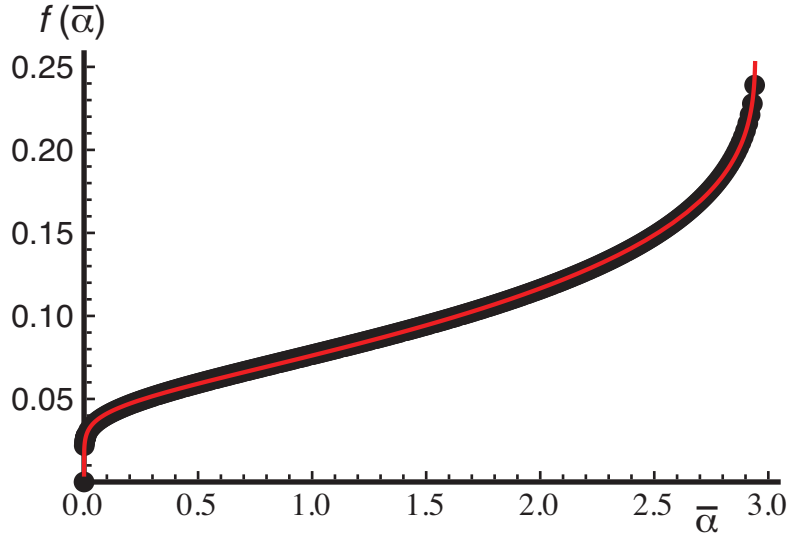


Figure 11. Plot of $f(\bar{\alpha})$, defined in equation (15), determined numerically (blue dots) and fitted with equation (16) (red line).

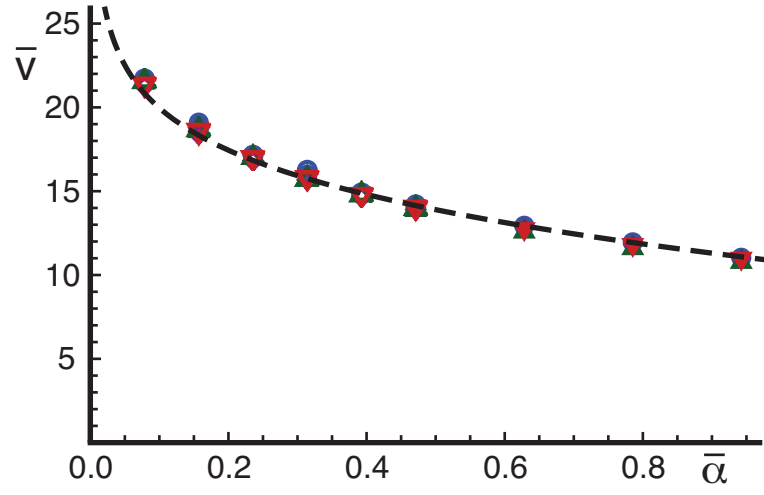


Figure 12. Dimensionless wavefront speed $\bar{v} = v/(D/a)$ as a function of the dimensionless threshold $\bar{\alpha} = 4\pi a^2 \alpha$ in the biochemical signaling model. The figure shows \bar{v} for several choices of the parameters D and a (different symbols). The data all collapse on a single curve, as described by equation (15). The dashed line is the fit to that curve of equation (16).

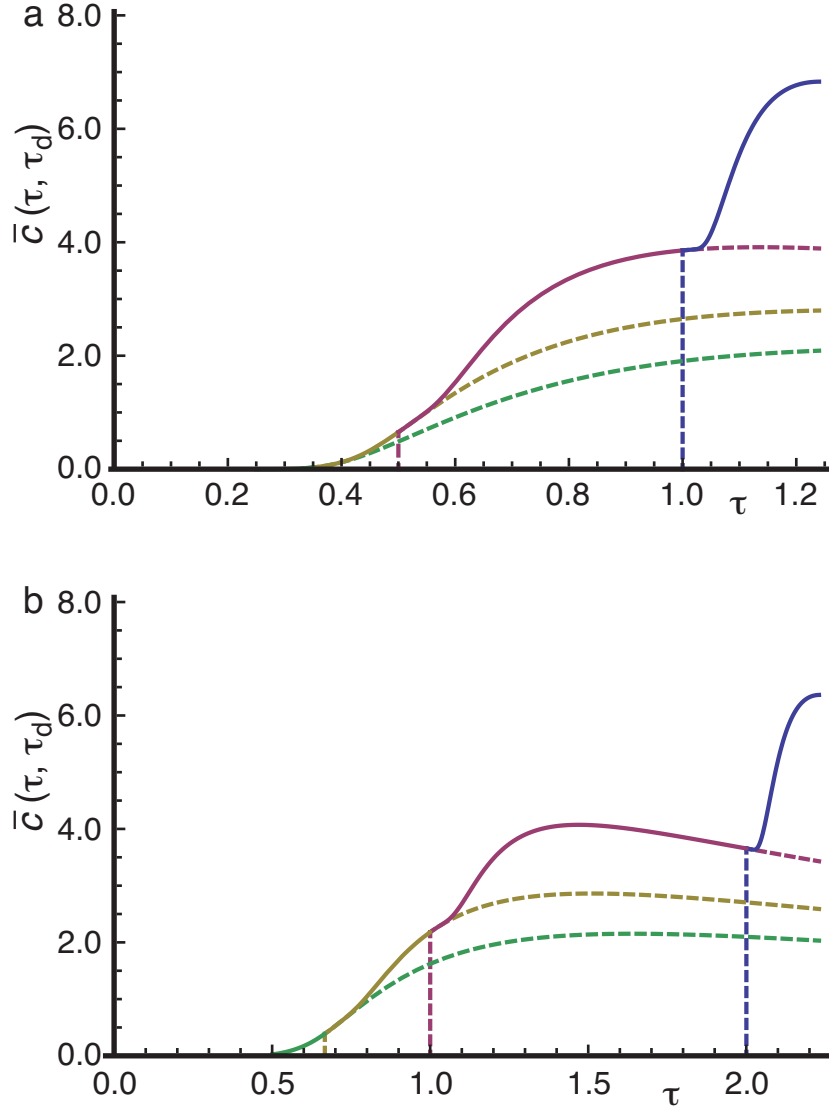


Figure 13. Plot of equation (17) for (a) $\tau_d = 1.0$ and (b) $\tau_d = 2.0$. The value of n_0 decreases with increasing τ , plotted values are 1 (blue), 2 (red), 3 (yellow) and 4 (green). Note that \bar{c} is a continuous function of τ , but not monotonous for larger values of τ_d .

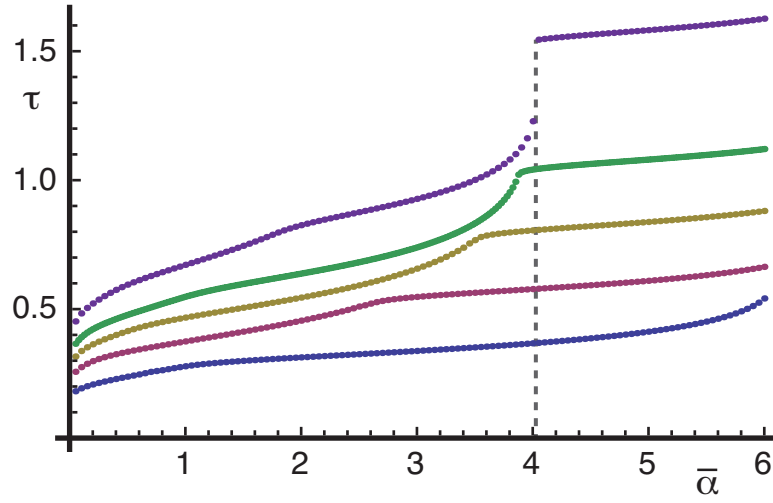


Figure 14. Time τ as a function of threshold value $\bar{\alpha}$ for several values of the delay time τ_d : 0.25 (blue), 0.50 (red), 0.75 (yellow), 1.0 (green), 1.50 (purple). Note that for larger values of τ_d , τ has a discontinuity because $c(\tau, \tau_d)$ is no longer monotonous. For smaller values, τ is continuous but does have a kink.

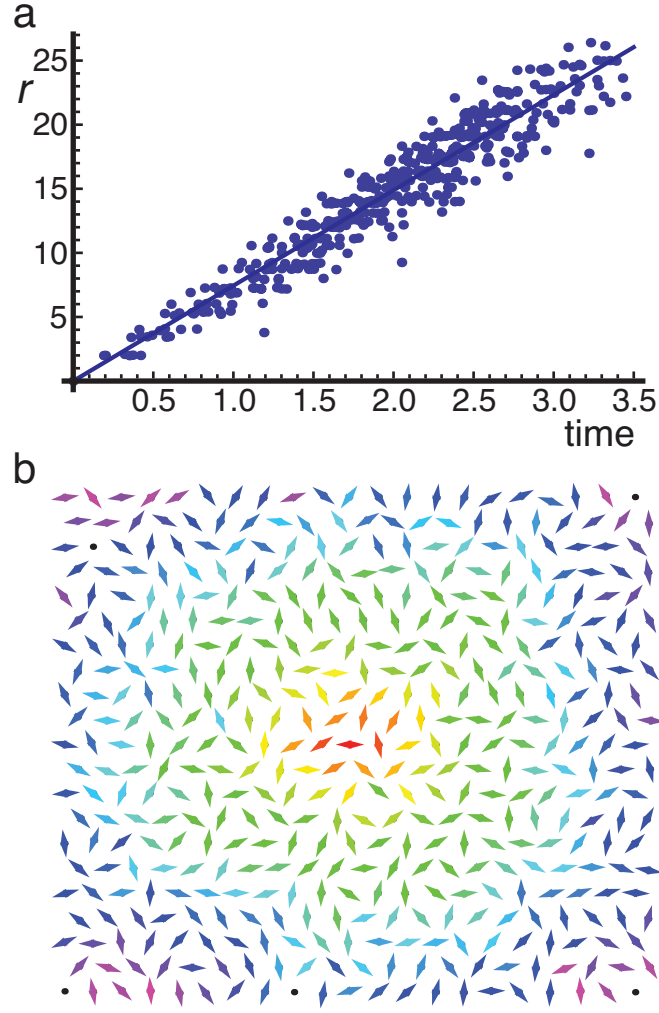


Figure 15. Wavefront from a simulation with 21×21 nuclei. The nuclei are arranged on a hexagonal grid with random small offsets. The wave starts at the center point which generates a stress dipole of unit strength along the x -axis at $t = 0$. Whenever the absolute value of the largest eigenvalue of the stress tensor at another nucleus exceeds the threshold value α , it also divides, adding a unit stress dipole in a random direction to the total stress field. a) Distance of the dividing nuclei to the center vs. their time, with a linear fit. b) Graphical representation of the 2 dimensional field, with the dipoles indicated in the orientation in which they divide, and color-coded according to the time that they divide, on a hue scale (red-yellow-green-blue-violet).